White light thermoplasmonic activated gold nanorod arrays enable the photo-thermal disinfection of medical tools from bacterial contamination

Federica Zaccagnini,[a] Piotr Radomski,[b] Maria Laura Sforza,[a] Pawel Ziółkowski,[b] Seok-In Lim,[c] Kwang-Un Jeong,[c] Dariusz Mikielewicz,[b] Nicholas P. Godman,[d] Dean R. Evans,[d] Jonathan E. Slagle,[d] Michael E. McConney,[d] Daniela De Biase,[a] Francesca Petronella *[e] and Luciano De Sio *[a]

[a]*Department of Medico-Surgical Sciences and Biotechnologies Sapienza University of Rome, Latina, Italy*

[b]*Gdansk University of Technology, Faculty of Mechanical Engineering and Ship Technology, Energy Institute, Poland*

[c]*Department of Polymer-Nano Science and Technology, Department of Nano Convergence Engineering, Jeonbuk National University, Jeonju, Republic of Korea*

[d]*US Air Force Research Laboratory, Wright-Patterson Air Force Base, Ohio, USA*

[e]*National Research Council of Italy, Institute of Crystallography CNR-IC, Area della Ricerca Roma 1 Strada Provinciale 35d, n. 9 - 00010 Montelibretti (RM)*

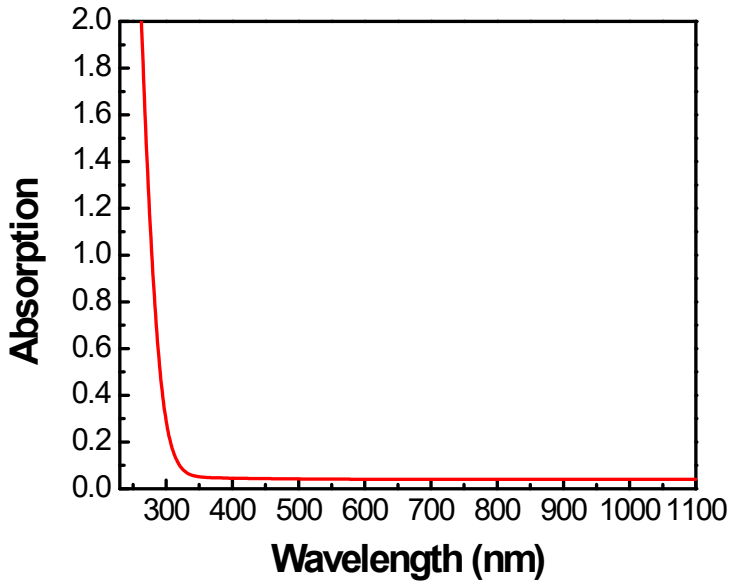

Figure SI 1 The spectral response of the glass substrate using air as the baseline. It is evident a very intense absorption below 300 nm.

1. Theoretical model

1.1. AuNRs optical coefficients

Optical cross sections, which are crucial to determining the absorption coefficient, are generally solved via two different methods – Mie-Lorentz theory and Rayleigh or Rayleigh-Drude approximation. The last one assumes that the light-nanoparticle interaction is described as dipoles carrying the charge whose arrangement is maximal if the nanoparticle and light frequencies are equal, which is called localized plasmonic resonance[1]. Mie-Lorentz's theory may be much more appropriate due to its enhanced accuracy, including multipole interactions. To define the nanoparticle's shape appropriately, however, this theory requires sophisticated mathematics whose solutions are generally followed with

long-time simulations unless it is a pure sphere. On the other hand, the Rayleigh-Drude approximation, although it imposes the conditions that $\frac{\lambda}{2\pi} > d_{NP}$, where d_{NP} is the AuNR size, appears to be a perfect verification for a wide number of shapes in IR- and Vis-ranges [2]'[3].

On the other hand, Rayleigh-Drude-approximation offers simpler solutions that may be solved without using numerical methods. The optical cross sections are introduced as:

$$C_{absi} = (C_{exti}) - (C_{scai}) = \left(4\pi \cdot \left(\frac{2\pi}{\lambda}\right) \cdot im(\alpha_i)\right) - \left(\frac{8\pi}{3} \cdot \left(\frac{2\pi}{\lambda}\right)^4 \cdot |\alpha_i|^2\right) \quad (1)$$

where:
C_{exti} – extinction cross section of the i-particle, m^2;
C_{scai} – scattering cross section of the i-particle, m^2;
C_{absi} – absorption cross section of the i-particle, m^2;
λ – incident wavelength, m;
α_i – total polarizability of the i-particle, m^2;
im – symbol of imaginary part

For the standard approach, the light-AuNR interaction is represented via polarizability functions of the dipole configurations, where the double-layered ellipsoids with an anisotropic depolarization factor $Л_i$ follow the formulas [2]'[4]:

$$\alpha_{i,x} = \frac{V_{1_i} + V_{2_i}}{4\pi} \cdot \frac{(\varepsilon_2 - \varepsilon_h)\cdot(\varepsilon_2 + (\varepsilon_1 - \varepsilon_2)\cdot(Л_{i,1,x} - \delta_i \cdot Л_{i,2,x})) + \delta_i \cdot \varepsilon_2 \cdot (\varepsilon_1 - \varepsilon_2)}{(\varepsilon_h + (\varepsilon_2 - \varepsilon_h)\cdot Л_{i,2,x})\cdot(\varepsilon_2 + (\varepsilon_1 - \varepsilon_2)\cdot(Л_{i,1,x} - \delta_i \cdot Л_{i,2,x})) + \delta_i \cdot Л_{i,2,x} \cdot \varepsilon_2 \cdot (\varepsilon_1 - \varepsilon_2)} \quad (2)$$

$$\alpha_{i,y} = \frac{V_{1_i} + V_{2_i}}{4\pi} \cdot \frac{(\varepsilon_2 - \varepsilon_h)\cdot(\varepsilon_2 + (\varepsilon_1 - \varepsilon_2)\cdot(Л_{i,1,y} - \delta_i \cdot Л_{i,2,y})) + \delta_i \cdot \varepsilon_2 \cdot (\varepsilon_1 - \varepsilon_2)}{(\varepsilon_h + (\varepsilon_2 - \varepsilon_h)\cdot Л_{i,2,y})\cdot(\varepsilon_2 + (\varepsilon_1 - \varepsilon_2)\cdot(Л_{i,1,y} - \delta_i \cdot Л_{i,2,y})) + \delta_i \cdot Л_{i,2,y} \cdot \varepsilon_2 \cdot (\varepsilon_1 - \varepsilon_2)} \quad (3)$$

$$\alpha_{i,z} = \frac{V_{1_i} + V_{2_i}}{4\pi} \cdot \frac{(\varepsilon_2 - \varepsilon_h)\cdot(\varepsilon_2 + (\varepsilon_1 - \varepsilon_2)\cdot(Л_{i,1,z} - \delta_i \cdot Л_{i,2,z})) + \delta_i \cdot \varepsilon_2 \cdot (\varepsilon_1 - \varepsilon_2)}{(\varepsilon_h + (\varepsilon_2 - \varepsilon_h)\cdot Л_{i,2,z})\cdot(\varepsilon_2 + (\varepsilon_1 - \varepsilon_2)\cdot(Л_{i,1,z} - \delta_i \cdot Л_{i,2,z})) + \delta_i \cdot Л_{i,2,z} \cdot \varepsilon_2 \cdot (\varepsilon_1 - \varepsilon_2)} \quad (4)$$

$$\delta_i = \frac{V_{1_i}}{V_{1_i} + V_{2_i}} \quad (5)$$

where:
$\alpha_{i,x}$ – polarizability of the i-particle along the x axis, m^3;
$\alpha_{i,y}$ – polarizability of the i-particle along the y axis, m^3;
$\alpha_{i,z}$ – polarizability of the i-particle along the z axis, m^3;
V_{1_i} – volume of the i-particle's core, m^3;
V_{2_i} – volume of the i-particle's shell, m^3;
ε_1 – complex function of the electrical permittivity of the core, here: gold permittivities, - ;
ε_2 – complex function of the electrical permittivity of the shell, here: CTAB permittivities, - ;
ε_h – complex function of the electrical permittivity of the surrounding medium, here: air, - ;
$Л_{i,1,x}$ – depolarization factor of the i-particle core along the x axis, - ;
$Л_{i,2,x}$ – depolarization factor of the i-particle shell along the x axis, - ;
$Л_{i,1,y}$ – depolarization factor of the i-particle core along the y axis, - ;
$Л_{i,2,y}$ – depolarization factor of the i-particle shell along the y axis, - ;

$Л_{i,1,z}$ – depolarization factor of the i-particle core along the z axis, - ;
$Л_{i,2,z}$ – depolarization factor of the i-particle shell along the z axis, -

The electrical permittivities are, in general, calculated via different Drude-model-based approaches. This work applies the Drude-CP model studied in [5] because it corresponds to many experiments. For prolate (stretched) structures, however, the depolarization factor should be specified via [2],[4]:

$$Л_i = \frac{1-{\phi_i}^2}{{\phi_i}^2}\cdot\left(\frac{1}{2\phi_i}\cdot\ln\left(\frac{1+\phi_i}{1-\phi_i}\right)-1\right) \tag{6}$$

$$\phi_i = \sqrt{1-\left(\frac{d_{si}}{d_{li}}\right)^2} \tag{7}$$

where:
d_{si} – short diameter of the i-particle, m;
d_{li} – long diameter of the i-particle, m

Contrary to ellipsoids, rods possess the long flat dimension, which contributes to appear new dipole configurations. Therefore, the depolarization factor that determines the dipole arrangement in an AuNR may be claimed to be a perfect parameter to solve and establish the other dipole configurations. It was discovered by Fuchs [51]. In His work, edgy shapes (triangles, cubes, octahedrons etc.) were determined numerically as weighted-$Л_i$ distributions. Considering of the two highest values of the depolarization factor in a cube, it may be realized that charge arrangements imply the uniform distributed ($Л_i \to \frac{1}{3}$) configuration and the one whose charges are arranged at the very opposite vertices along a cube space diagonal ($Л_i(d_{si},d_{li}) \to Л_i(d_{si},d_{si}\sqrt{3})$).

A similar arrangement is exploited for the AuNRs; however, depolarization factors are adopted for the prolation factors, ϕ_i, and are transformed into:

$$\phi_i(d_{si},d_{li}) \to \phi_{i,dl}\left(d_{li}-d_{si},\sqrt{(d_{li}-d_{si})^2+(d_{si})^2}\right) \tag{8}$$

$$\phi_i(d_{si},d_{li}) \to \phi_{i,ds}\left(d_{si},\sqrt{(d_{li}-d_{si})^2+(d_{si})^2}\right) \tag{9}$$

for y- and x-, z- axes respectively. Figure SI 2 demonstrates these four assumed charge arrangements that have been adjusted to the x-oriented AuNRs.

Nonetheless, the platform-deposited particles are also governed by the particle-surface interaction. This situation is assumed differently from the other configurations due to the outer electrical field distribution from the interaction between two different compounds – AuNR and the PE layer. So far, many papers have been published about the issue where the AuNPs are dispersed in a solution, and only a few explain precisely how the interaction may be treated [2],[7],[8],[9] once immobilized on a surface. Moreover, none of them deal with elongated shapes due to the high complexity of the problem. This work introduces the surface effect as the interaction between AuNRs and the PE layer that is considered a flat disk.

Basing on Royer's and Yamaguchi's approaches: [2],[10]:

$$(\alpha_{i,x})_{sur} = \left(\frac{-\left(\frac{d_{si}}{2}\right)^3\cdot\left(\frac{1-{\phi_i}^2}{{\phi_i}^2}\right)^{\frac{1}{2}}}{3\cdot q_{11}\left(i\cdot\left(\frac{1-{\phi_i}^2}{{\phi_i}^2}\right)^{\frac{1}{2}}\right)}\cdot\frac{\varepsilon_1-\varepsilon_h}{\varepsilon_1-e_{11}\left(i\cdot\left(\frac{1-{\phi_i}^2}{{\phi_i}^2}\right)^{\frac{1}{2}}\right)}\right) \tag{10}$$

$$(\alpha_{i,y})_{sur} = \left(\frac{2 \cdot \left(\frac{d_{si}}{2}\right)^3 \cdot \left(\frac{1}{\phi_i}\right)}{3 \cdot q_{10}\left(i \cdot \left(\frac{1-{\phi_i}^2}{{\phi_i}^2}\right)^{\frac{1}{2}}\right)} \cdot \frac{\varepsilon_1 - \varepsilon_h}{\varepsilon_1 - e_{10}\left(i \cdot \left(\frac{1-{\phi_i}^2}{{\phi_i}^2}\right)^{\frac{1}{2}}\right)} \right) \tag{11}$$

$$(\alpha_{i,z})_{sur} = \left(\frac{2 \cdot \left(\frac{d_{si}}{2}\right)^3 \cdot \left(\frac{1}{\phi_i}\right)}{3 \cdot q_{11}\left(i \cdot \left(\frac{1-{\phi_i}^2}{{\phi_i}^2}\right)^{\frac{1}{2}}\right)} \cdot \frac{\varepsilon_1 - \varepsilon_h}{\varepsilon_1 - e_{11}\left(i \cdot \left(\frac{1-{\phi_i}^2}{{\phi_i}^2}\right)^{\frac{1}{2}}\right)} \right) \tag{12}$$

$$e_{\Lambda \mathrm{M}} = \frac{p_{\Lambda \mathrm{M}}\left(i \cdot \left(\frac{1-{\phi_i}^2}{{\phi_i}^2}\right)^{\frac{1}{2}}\right) \cdot \left(\frac{dq_{\Lambda \mathrm{M}}(i \cdot \psi)}{d\psi}\right)_{\psi = \left(\frac{1-{\phi_i}^2}{{\phi_i}^2}\right)^{\frac{1}{2}}}}{q_{\Lambda \mathrm{M}}\left(i \cdot \left(\frac{1-{\phi_i}^2}{{\phi_i}^2}\right)^{\frac{1}{2}}\right) \cdot \left(\frac{dp_{\Lambda \mathrm{M}}(i \cdot \psi)}{d\psi}\right)_{\psi = \left(\frac{1-{\phi_i}^2}{{\phi_i}^2}\right)^{\frac{1}{2}}}} \tag{13}$$

where:

$p_{\Lambda \mathrm{M}}$ and $q_{\Lambda \mathrm{M}}$ – associated Legendre polynomials of a first and a second kind, respectively;

Λ , M – orientation modes with respect to a surface

Adopting the formulas to the considered system from Royer et al.[2], the oscillation modes, Λ and M, refer to the particle's orientation. Hence, each electrical dipole perpendicular to the surface (or projected on y axis) corresponds to the situation in which $\Lambda = 1$, $M = 0$. On the other hand, for x and z axes, charges are not directed towards the surface, thus every mode equals 1.

The surface interaction, however, is also coupled with the distance between particles. From Yamaguchi's [44,50] approach, the nanoparticle distance is governed by the following:

$$(\alpha_{i,x})_{Ya} = \frac{(\alpha_{i,x})_{sur}}{1 + \left(\frac{(\alpha_{i,x})_{sur}}{\frac{4}{3}\pi \cdot {d_{si}}^2 \cdot d_{li}}\right) \cdot \beta_{||_i}} \tag{14}$$

$$(\alpha_{i,y})_{Ya} = \frac{(\alpha_{i,y})_{sur}}{1 + \left(\frac{(\alpha_{i,y})_{sur}}{\frac{4}{3}\pi \cdot {d_{si}}^2 \cdot d_{li}}\right) \cdot \beta_{\perp_i}} \tag{15}$$

$$(\alpha_{i,z})_{Ya} = \frac{(\alpha_{i,z})_{sur}}{1 + \left(\frac{(\alpha_{i,z})_{sur}}{\frac{4}{3}\pi \cdot {d_{si}}^2 \cdot d_{li}}\right) \cdot \beta_{||_i}} \tag{16}$$

$$\beta_{||_i} = \frac{\frac{4}{3}\pi \cdot {d_{s1i}}^2 \cdot d_{l1i}}{\varepsilon_{sur} + \varepsilon_h} \cdot \left(\frac{-(\varepsilon_{sur} - \varepsilon_h)}{(d_{s1i} + d_{s2i})^3} + \frac{2}{\varepsilon_o \cdot \varepsilon_h} \cdot \sum_{l}^{\binom{N}{2}} \frac{\left(1 - 3 \cdot \left(\frac{u_l}{\sqrt{{u_l}^2 + (d_{s1i} + d_{s2i})^2}}\right)^2\right)}{{u_l}^3} \right) \quad (17)$$

$$\beta_{\perp_i} = \frac{\frac{4}{3}\pi \cdot {d_{s1i}}^2 \cdot d_{l1i}}{\varepsilon_{sur} + \varepsilon_h} \cdot \left(\frac{-2 \cdot (\varepsilon_{sur} - \varepsilon_h)}{4\pi \cdot \varepsilon_o \cdot \varepsilon_h \cdot (d_{s1i} + d_{s2i})^3} + \frac{2 \cdot \varepsilon_{sur}}{\varepsilon_o \cdot \varepsilon_h} \cdot \sum_{l}^{\binom{N}{2}} \left(\frac{1}{{u_l}^3}\right) \right) \quad (18)$$

where:

$p_{\Lambda M}$ and $q_{\Lambda M}$ – associated Legendre polynomials of a first and a second kind, respectively;

Λ , M – oscillation modes;

d_{s1i} and d_{l1i} – short and long dimension of the internal layer, here: gold, m;

d_{s2i} – thickness of the capping agent (CTAB), m;

u_l – NR – NR semidistance from their centers (is identical to the surface disk dimensions): here: ~ 98.5 for x- and $\sim 78.5\ nm$ for z-projected axis;

$\beta_{||_i}$ – Yamaguchi's coefficient for parallel contribution to the surface effect;

$\beta_{\perp_i}$ – Yamaguchi's coefficient for perpendicular contribution to the surface effect;

l refers to the pair of the i- and $(i+1)$-particle, up to the $\binom{N}{2}$ pairs;

ε_{sur} – permittivity of surface, here: PE material;

ε_o – vacuum permittivity, $F \cdot m$

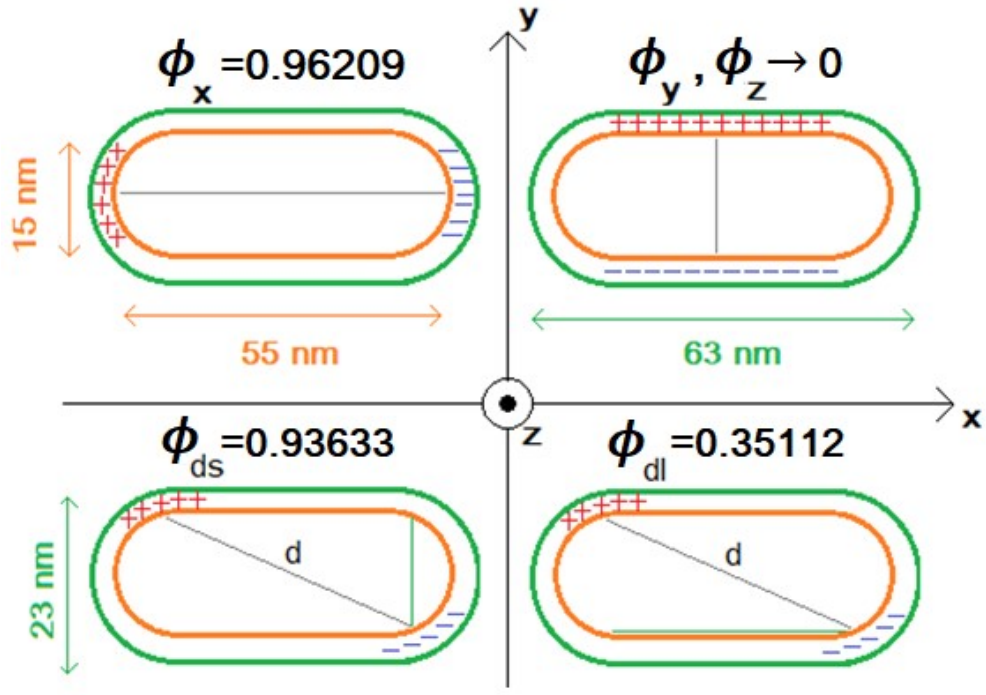

Figure SI 2. Electric dipole configurations that have been considered in the calculations for 15-15-55-nm gold nanorods (orange color) coated by a 4-nm CTAB compound (green color)

It is worth emphasizing that for dense-packed AuNRs, the formulas (1)(8)-(18) require to be improved with the AuNR-AuNR multipole interactions, e.g., based on the Lorentz-Lorenz or Mie theory [10]. However, the AuNRs are considered

sufficiently remote to include this relationship in this work. The total polarizability also requires some special conditions that are due to the particle's symmetry, and they are specified with the one following equation [2]:

$$\alpha_i = \frac{2}{3}\left(\frac{2}{3}\cdot\left((\alpha_{i,y})_{Ya} + (\alpha_{i,z})_{Ya}\right) + \frac{1}{3}\cdot\left((\alpha_{i,x,dl})_{Ya}\right)\right) + \frac{1}{3}\cdot\left(\frac{2}{3}\cdot\left((\alpha_{i,y,ds})_{Ya} + (\alpha_{i,z,ds})_{Ya}\right) + \frac{1}{3}\cdot\left((\alpha_{i,x})_{Ya}\right)\right) \quad (19)$$

where:
$(\alpha_{i,x,dl})_{Ya}$ – surface polarizability of the i-particle along the rod space diagonal projected on the x axis, m^3;
$(\alpha_{i,y,ds})_{Ya}$ – surface polarizability of the i-particle along the rod space diagonal projected on the y axis, m^3;
$(\alpha_{i,z,ds})_{Ya}$ – surface polarizability of the i-particle along the rod space diagonal projected on the z axis, m^3.

For other shapes, like cubes or triangles, the fractions vary considerably, and frequently, numerical methods need to be used.

1.2. Temperature distributions

The temperature increase is generally calculated thanks to the standard mass, momenta, and energy balance equations [13]'[14]:

$$\frac{\partial}{\partial t}\begin{Bmatrix}\rho\\ \rho\vec{v}\\ \rho e\end{Bmatrix} + div\begin{Bmatrix}\rho\vec{v}\\ \rho\vec{v}\otimes\vec{v}\\ \rho e\vec{v}\end{Bmatrix} + div\begin{Bmatrix}0\\ p\overleftrightarrow{I}\\ p\vec{v}\end{Bmatrix} = div\begin{Bmatrix}0\\ \overleftrightarrow{\tau}\\ \overleftrightarrow{\tau}\cdot\vec{v} + \vec{q}\end{Bmatrix} + \begin{Bmatrix}0\\ \rho\cdot\vec{S}_{\vec{v}}\\ \breve{S}_e^{\,TOT}\end{Bmatrix} \quad (20)$$

$$\overleftrightarrow{\tau} = grad\left(\vec{X}^t\right) - \frac{2}{3}\mu I_{\vec{d}}\overleftrightarrow{I} + 2\mu\overleftrightarrow{d} = grad\left(\frac{d\overleftrightarrow{\sigma}}{dT}\cdot grad(T)\right) - \frac{2}{3}\mu I_{\vec{d}}\overleftrightarrow{I} + 2\mu\overleftrightarrow{d} \quad (21)$$

where:
t – time, s;
ρ – density (here: water), $kg\cdot m^{-3}$;
e – specific energy, $J\cdot kg^{-1}$;
c_p – specific heat capacity, $J\cdot kg^{-1}\cdot K^{-1}$
$\vec{v}$ – velocity of the fluid, $m\cdot s^{-1}$;
$\vec{q}$ – Fourier heat flux;
$\overleftrightarrow{\tau}$ – total momentum flux, Pa;
$\overleftrightarrow{I}$ – unit tensor;
p – pressure, Pa;
$\vec{X}^t$ – diffusive momentum flux; Pa
$\frac{d\overleftrightarrow{\sigma}}{dT}$ – surface tension gradient, $N\cdot m^{-1}\cdot K^{-1}$, here: $-0.05263\ mN\cdot m^{-1}\cdot K^{-1}$;
T – temperature, K;
$\vec{S}_{\vec{v}}$ – momentum source term, here: gravity;
$\breve{S}_e^{\,TOT} = S_e^M + S_e^{NP}$ – total source of energy, $W\cdot m^{-3}$;
$\breve{S}_e^M$ – source of energy for continuous materials, $W\cdot m^{-3}$;
$\breve{S}_e^{NP}$ – source of energy for nanoparticles, $W\cdot m^{-3}$.

Curved geometries, however, also require including the radiative transport equation that is generally calculated using the DOM model. Due to the high-simulation time, however, this work assumes another model that has been proposed in [11]'[12]'[15]. The presence of AuNRs is here treated as a boundary condition, and the whole absorbed part of the irradiation is directly responsible for the heat conversion rate, following the formulas:

$$S_e^{NP} = \sum_{i=1}^{N} \sigma_{absi} \cdot I_{absi} = \xi \cdot \sum_{i}^{N} (w_i \cdot C_{absi}) \cdot I_{absi} =$$
$$= \xi \cdot \sum_{i}^{N} (w_i \cdot C_{absi}) \cdot I_o \cdot (1 - R_{CTAB}) \cdot (1 - R_g) \cdot \left(1 - \exp\left(\left(-\xi \cdot \sum_{i}^{N} (w_i \cdot C_{absi}) \cdot l_{p-h}\right)\right)\right) \quad (22)$$

$$I_o = \left(J_o(\lambda) \cdot max(I_o)\right) \cdot \exp\left(-2 \cdot \left(\frac{\vec{r}}{d_B}\right)^2\right) \quad (23)$$

$$R_{CTAB} = \left(\frac{n_{CTAB} - n_h(\lambda)}{n_{CTAB} + n_h(\lambda)}\right)^2 \quad (24)$$

$$R_g = \frac{\left(\sqrt{\frac{|\varepsilon_g| + im\left(\varepsilon_g\right)}{2}} - n_{CTAB}\right)^2 + \left(\sqrt{\frac{|\varepsilon_g| - im\left(\varepsilon_g\right)}{2}}\right)^2}{\left(\sqrt{\frac{|\varepsilon_g| + im\left(\varepsilon_g\right)}{2}} + n_{CTAB}\right)^2 + \left(\sqrt{\frac{|\varepsilon_g| - im\left(\varepsilon_g\right)}{2}}\right)^2} \quad (25)$$

where:

I_{absi} – absorbed part of irradiation, $W \cdot m^{-2}$;

I_o – incident irradiation, $W \cdot m^{-2}$;

$J_o(\lambda)$ – incident irradiation function in reduced-to-one units, $W \cdot m^{-2}$;

R_{CTAB} – reflected coefficient of the CTAB compound, - ;

R_g – reflected coefficient of the gold material, - ;

l_{p-h} – penetration depth, here: 26.0 nm ;

P – output power of laser, W ;

d_B – beam size, m ;

$\vec{r}$ – radial distance, m ;

n_{CTAB} – refractive index of the CTAB compound, - ;

$n_h(\lambda)$ – wavelength function of either the 15%-humid-air or NOA-61 refractive index, - ;

$\varepsilon_g \equiv \varepsilon_1$ – complex function of the electrical permittivity of gold, - ;

$|\varepsilon_g|$ – absolute value of the electrical permittivity of gold, - .

This is the situation when the AuNRs are irradiated with a monochromatic light source. The problem appears if the incident irradiation characterizes an asymmetrical spectra distribution (e.g. solar light). In this paper, the authors suggest that the heat generation rate would be transformed into $S_e^{NP} \rightarrow \breve{S}_e^{NP}$ and $S_e^{M} \rightarrow \breve{S}_e^{M}$ which are described as:

$$\breve{S}_e^{NP} = \frac{\int_{\lambda_o}^{\lambda_k} S_e^{NP} d\lambda}{\int_{\lambda_o}^{\lambda_k} d\lambda} \quad (26)$$

$$\breve{S}_e^M = \frac{\int_{\lambda_o}^{\lambda_k} S_e^M d\lambda}{\int_{\lambda_o}^{\lambda_k} d\lambda} \tag{27}$$

where:

λ_o – lower limit of the wavelength interval, here: 250 nm;

λ_k – upper limit of the wavelength interval, here: 1100 nm.

Using discrete numbers, the integral from the formulas (26) and (27) become a sum from λ_o to λ_k.

As long as the l_{p-h} is treated as a thin surface with the AuNRs as inclusions, the situation is significantly different for the continuous materials where the beam is diminished as the depth increases. Therefore, the l_{p-h} is then transformed into the function of the light ray line, yielding the considered system [12]'[15]:

$$S_e^M = \sigma_{abs_M} \cdot I_{abs_M} = \sigma_{abs_M}(\lambda) \cdot I_o(\lambda) \cdot (1 - R_M(\lambda)) \cdot (1 - \exp\left(-\sigma_{abs_M}(\lambda) \cdot d_M\right) \tag{28}$$

$$\sigma_{abs_M}(\lambda) = \frac{4\pi \cdot im(n_M(\lambda))}{\lambda} \tag{29}$$

$$R_M(\lambda) = \frac{\left(re(n_M(\lambda)) - n_{air}(\lambda)\right)^2 + \left(im(n_M(\lambda))\right)^2}{\left(re(n_M(\lambda)) + n_{air}(\lambda)\right)^2 + \left(im(n_M(\lambda))\right)^2} \tag{30}$$

where:

$\sigma_{abs_M}(\lambda)$ – wavelength function of the absorption coefficient of a material, m^{-1};

I_{abs_M} – the part of the irradiation that has been absorbed by a material, $W \cdot m^{-2}$;

$I_o(\lambda)$ – spectral distribution of the light source's power density, $W \cdot m^{-2}$;

$R_M(\lambda)$ – wavelength function of the reflection coefficient of a material, - ;

d_M – optical thickness in the considered material, m;

$n_M(\lambda)$ – wavelength function of the refractive index of a material, - ;

re – real part of a parameter

All the abovementioned equations have been investigated and adjusted to the working system. Moreover, the appropriate boundary conditions have to be specified, which is deliberated in Section 2.

2. Calculation methods and boundary conditions

Both optical cross-sections and temperature distributions are determined using two different techniques. Nevertheless, the absorption coefficient and the properties of the surrounding medium do the lion's share in heat and mass transfer. The absorption cross sections are calculated analytically based on the Rayleigh-Drude approximation following the formulas (1) – (19) and (21) – (30). All calculations have been examined in the *Wolfram.Mathematica* software (version 11.3.0). The nanoparticle size and shape distributions are included for $N = 130\ x\ 130 = 16900$ dimension groups based on the Gaussian curves where the maximum value has been located at the 15 x 15 x 55 nm size. The material parameters are specified in table 2.1 in the range from 250 to 1100 nm.

Table 2.1. Assumed parameters for absorption spectra calculations

Parameters		**Assumed value**	**References**
NPs size, d_{s1} x d_{s1} x d_{l1}		15 x 15 x 55 nm	-
Thickness of the capping agent (CTAB), d_{s2}		4 nm	-
Average NR – NR distance		142 nm	-
Nanoparticles density, ξ		$8.67 \cdot 10^{21}$ m^{-3}	-
Fluid refractive index, n_h	air (humidity – 15%)	1.04660[1]	[16]
	NOA-61	1.55935[1]	[17]
	water	1.33200[1]	[18]
Refractive index of PE platform, n_{sur}		1.50806[1]	[10],[19],[20]
Refractive index of borosilicate glass, n_{glass}		1.51630[1]	[21]
Refractive index of CTAB compound, n_{CTAB}		1.44000	[22]
Electrical permittivity, $\varepsilon_g = \varepsilon_1$	re	- 9.34832[1]	[5]
	im	1.33190[1]	

On the other hand, the temperature distributions are determined using CFD methods and algorithms following the formulas (20) – (21). The calculations have been performed via *Ansys.Fluent* software (version 22.1) using the *Tryton* supercomputer of the TASK resources of 72 cores (Intel®Xeon®Processor E5 v3 @ 2,3 GHz).

Figure SI 3 demonstrates the geometry reproduced based on the experiments, whereas meshes and their specifications are revealed in *Appendix A*. The simulations are run using the SIMPLE algorithm and the second-order scheme for the general (20) equations. The control parameters are established at 0.5, except pressure and density, whose values equal 0.3. Before the simulations start, materials properties and boundary conditions have been specified for the considered system, which is highlighted in Tables 2.2 and 2.3. Due to the lack of some parameters about the NOA-61 glue, epoxy resin has been adjusted.

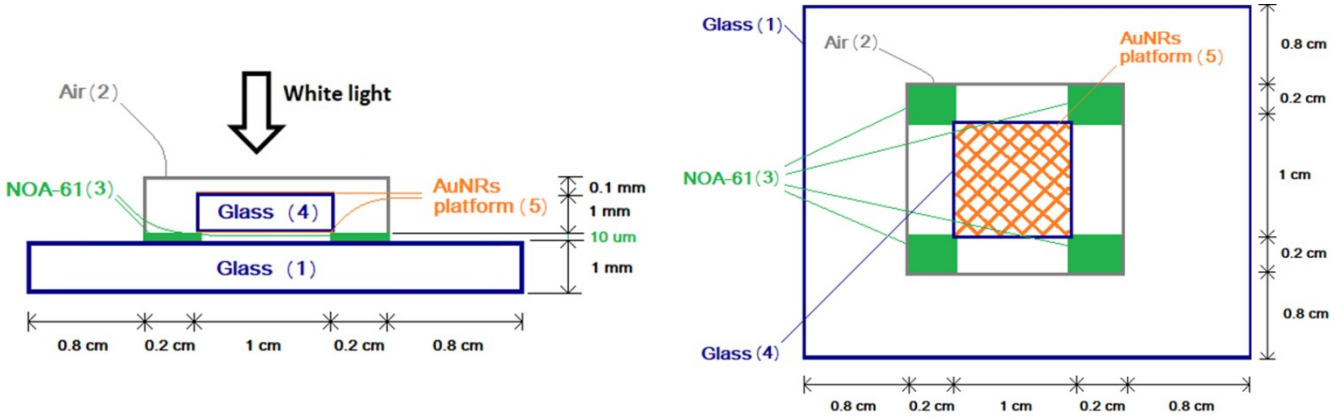

Figure SI 3. Scheme of the reproduced geometry applied in the simulations (scale has not been saved)

[1] At standard conditions: λ=600 nm, p=1 atm T_o=24°C

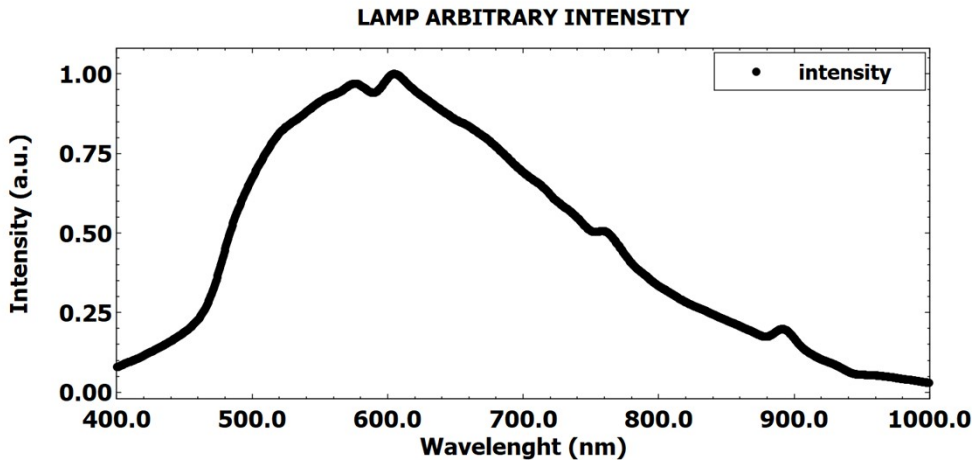

Figure SI 4. Intensity spectrum distribution $J_o(\lambda)$ of the applied lamp

Table 2.2. Material properties in the considered simulations

Material	**Density** $(kg{\cdot}m^{-3})$	**Specific heat capacity** $(J{\cdot}kg^{-1}{\cdot}K^{-1})$	**Thermal conductivity coefficient** $(W{\cdot}m^{-1}{\cdot}K^{-1})$	**Dynamic viscosity** $(Pa{\cdot}s)$	**References**
Borosilicate glass	2124.9	779.74	$0.9245251 + 0.0004777689{\cdot}T + 9.178795{\cdot}10^{-7}{\cdot}T^2$	-	[21],[23]
Gold	19320	129.81	317	-	[24],[25]
Air	$352.965{\cdot}T^{-1}$	1006.43	$0.004204762 + 7.242857{\cdot}10^{-5}{\cdot}T$	$7.29{\cdot}10^{-6} + 4.0{\cdot}1$	[26],[27],[28]
NOA61	1231	1100	0.50	0.30	[17],[29]

Table 2.3. Specified boundary conditions in the considered simulations

No.	**Material**	**Type of boundary conditions**	**Details**	**Formulas & equations**	**References**
(1)	Bottom borosilicate glass	Mixed	$T_o = 297.15\ K\ (75.20^oF)$ $h_{glass-air} = 13.6\ W{\cdot}m^{-2}{\cdot}K^{-1}$ $d_M = 0.001\ m$ $max(I_o) = 286000\ W{\cdot}m^{-2}$ $\max\left(S_e^M\right) = 347.75\ W{\cdot}m^{-3}$ $d_B = 0.004\ m$	(15) (22) – (25)	[21],[23]
(2)	Air	Outlet (Neumann)	$T_o = 297.15\ K\ (75.20^oF)$ $v_o = 0$	(15)	-
(3)	NOA61	Neumann	$T_o = 297.15\ K\ (75.20^oF)$ $\dot{q} = 0\ W{\cdot}m^{-2}$	(15)	-
(4)	Top borosilicate glass	Mixed	$T_o = 297.15\ K\ (75.20^oF)$ $h_{glass-air} = 13.6\ W{\cdot}m^{-2}{\cdot}K^{-1}$ $d_M = 0.001\ m$ $max(I_o) = 286000\ W{\cdot}m^{-2}$ $\max\left(S_e^M\right) = 1.2057{\cdot}10^6\ W{\cdot}m^{-3}$ $d_B = 0.004\ m$	(15) (21) – (24)	[21],[23]
(5)	Gold surface	Neumann	$T_o = 297.15\ K\ (75.20^oF)$	(1) – (20)	[2],[11],[12],[24]

			$l_{p-h} = 26.0\ nm$ $max(I_o) = 286000\ W{\cdot}m^{-2}$ $max(S_e^{NP}) = 1.0778{\cdot}10^{11}\ W{\cdot}m^{-3}$ $d_B = 0.004\ m$		

3. References

[1] L. De Sio, T. Placido, R. Comparelli, M. Lucia Curri, M. Striccoli, N. Tabiryan, T. J. Bunning, *Progress in Quantum Electronics* **2015**, 41, 23.

[2] C. F. Bohren, D. R. Huffman, *Absorption and scattering of light by small particles*, **1983**.

[3] G. Mie, *Annalen der Physik* **1908**, 330, 377.

[4] A. Sihvola, I. V. Lindell, *Journal of Electromagnetic Waves and Applications* **1990**, 4, 1.

[5] A. Vial, T. Laroche, *Journal of Physics D: Applied Physics* **2007**, 40, 7152.

[6] R. Fuchs, *Physical Review B* **1975**, 11, 1732.

[7] T. Yamaguchi, S. Yoshida, A. Kinbara, *Thin Solid Films* **1974**, 21, 173.

[8] P. Royer, J. L. Bijeon, J. P. Goudonnet, T. Inagaki, E. T. Arakawa, *Surface Science* **1989**, 217, 384.

[9] P. Royer, J. P. Goudonnet, R. J. Warmack, T. L. Ferrell, *Physical Review B* **1987**, 35, 3753.

[10] J. P. Toennies, *Optical Properties of Metal Clusters*, Springer-Verlag, Germany **1995**.

[11] P. Radomski, P. Ziółkowski, L. De Sio, D. Mikielewicz, *Archives of Thermodynamics* **2021**, 42, 87.

[12] P. Radomski, P. Ziółkowski, D. Mikielewicz, *Theoretical approach of laser-irradiated metallic nanoparticles in selected mixed-convection systems*, Proceedings in heat and mass transfer reseach. Conference monography of XVI Heat and Mass Transfer Symposium, Polish Academy of Science (PAN), Bialystok 2022, 374-384, DOI: 10.24427/978-83-67185-30-1_38.

[13] P. Ziółkowski, J. Badur, *International Journal of Numerical Methods for Heat & Fluid Flow* **2017**, 28, 00.

[14] P. Ziółkowski, *AIP Conference Proceedings* **2019**, 2077, 020065.

[15] S. E. Black, *Laser ablation: Effects and applications*, **2011**.

[16] E. Bengt, *Metrologia* **1966**, 2, 71.

[17] N. P. Incorporate, 1999.

[18] R. Fernández-Prini, presented at *The International Association for the Properties of Water and Steam*, Erlangen, Germany, **1997**.

[19] C.-W. Chen, S.-Y. Hsiao, C.-Y. Chen, H.-W. Kang, Z.-Y. Huang, H.-W. Lin, *Journal of Materials Chemistry A* **2015**, 3, 9152.

[20] T. A. A. Laboratory.

[21] N. P. Bansal, R. H. Doremus, in *Handbook of Glass Properties*, (Eds: N. P. Bansal, R. H. Doremus), Academic Press, San Diego 1986.

[22] C. J. Murphy, T. K. Sau, A. M. Gole, C. J. Orendorff, J. Gao, L. Gou, S. E. Hunyadi, T. Li, *The journal of physical chemistry. B* **2005**, 109, 13857.

[23] M. P. Zaitlin, A. C. Anderson, *Physical Review Letters* **1974**, 33, 1158.

[24] H. Reddy, U. Guler, A. V. Kildishev, A. Boltasseva, V. M. Shalaev, *Opt. Mater. Express* **2016**, 6, 2776.

[25] R. Siegel, J. R. Howell, M. P. Mengüç, **2020**.

[26] Engineering ToolBox 2003.

[27] Engineering ToolBox 2009.

[28] Engineering ToolBox 2003.

[29] J. E. Mark, **2009**.

[30] V. M. Carrillo R, J. E. Petrie, E. A. Pacheco, *Maskana* **2016**, 5, 115.

[31] P. J. Roache, *Annual Review of Fluid Mechanics* **1997**, 29, 123.

Appendix A: Mesh and time independent tests

This part demonstrates the mesh and time independence procedure based on Richardson's and Roache's extrapolations. The first one allows the determination of the continuum values of a selected quantity f_{ext} and highlights the relative and fractional error between the different mesh or timestep results. Moreover, this approach is dedicated to lower-order discrete values. The methodology is bases on the formula[30]:

$$f_{ext} = f_{h=0} + g_1 \cdot h + g_2 \cdot h^3 + \ldots \tag{A1}$$

where:
ϵ – relative error between two sets/values of data, - ;
$f_{1,2,3,\ldots}$ – value for the 1st , 2nd, 3rd set of data,
$f_{h=0}$ – continuum value as if the mesh or time size equals zero)
$g_{1,2,3,\ldots}$ – constant or a function of the selected parameter that is other than h

For the second-order scheme that has been utilized in this work the continuum value $f_{h=0}$ yields:

$$f_{h=0} = f_1 + \frac{f_2 - f_1}{\left(\frac{h_2}{h_1}\right)^{\delta} - 1} \tag{A2}$$

where:
$h_{1,2,3,\ldots}$ – 1st , 2nd , 3rd … grid or time size;
δ – rank of accuracy, here: $\delta = 2$

Accordingly, the equation (A2) is transformed for three meshes into:

$$f_{ext} = \frac{2^n \cdot f_1 - f_2}{2^n - 1} \tag{A3}$$

$$n = \log_2\left(\frac{f_2 - f_3}{f_1 - f_2}\right) \tag{A4}$$

which allows the investigated value to be extrapolated with a specified error, e.g., the relative ϵ and fractional error E_1 between two sets of data that follow:

$$\epsilon = \frac{f_2 - f_1}{f_1} \tag{A5}$$

$$E_1 = \frac{\epsilon}{\left(\frac{h_2}{h_1}\right)^{\delta} - 1} \tag{A6}$$

Furthermore, Roache's approach[31] has introduced the grid convergence index (GCI) methodology that indicates how far the error may change as the mesh is finer, which for Richardson extrapolation is defined by the GCI parameter:

$$GCI_{(fine)} = F_s \cdot |E_1| = F_s \cdot \frac{|\epsilon|}{\left(\frac{h_2}{h_1}\right)^{\delta} - 1} \tag{A7}$$

where:
F_s – factor of safety, here: 1.25

In this work, three meshes are consumed so as to provide the mesh and timestep to be independent. Figure A01 reveals the discretization used, whereas Table TA01 highlights the details of these grids. As the quantity value, two parameters have been selected – the maximum temperature in the whole system (*max*) and top glass (4) mean temperature (*mean*) have been utilized for the Richardson extrapolation and GCI methodology, both in spatial and time regimes. The obtained comparison are reported in Figure A01 , whereas the error data are included in Table TA02.

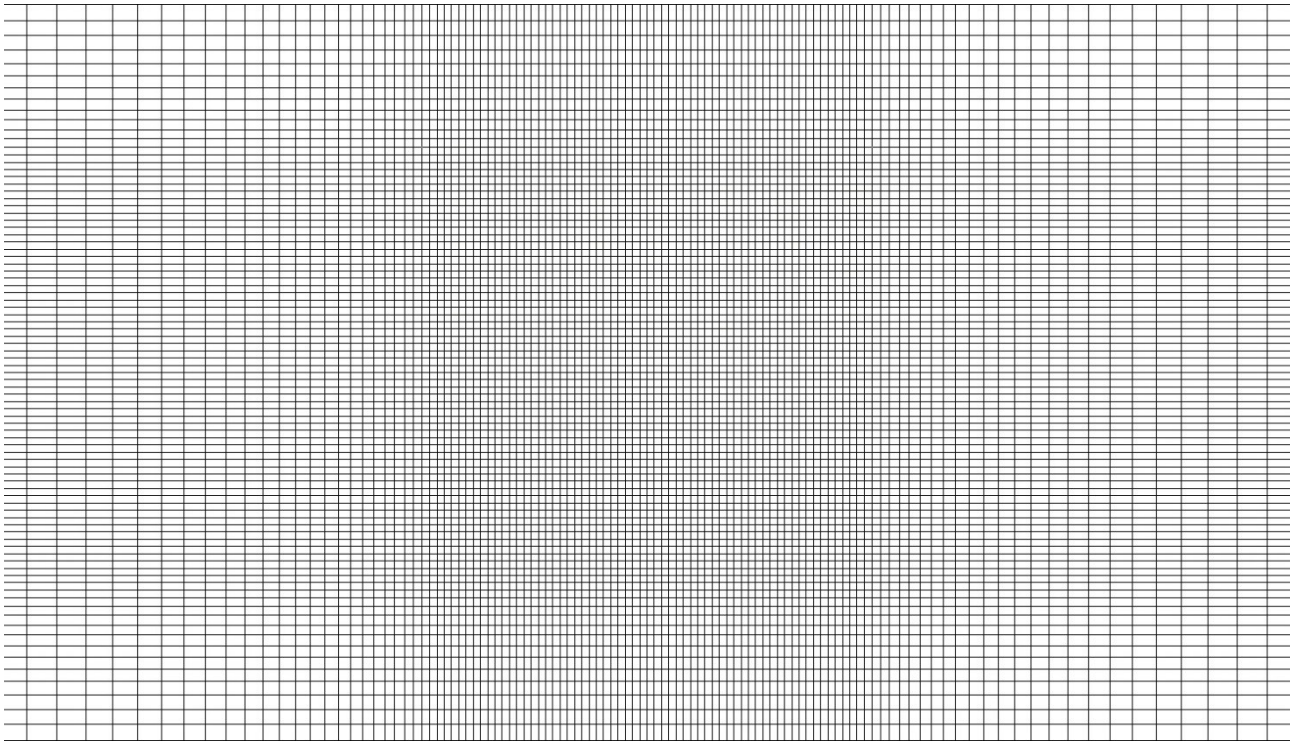

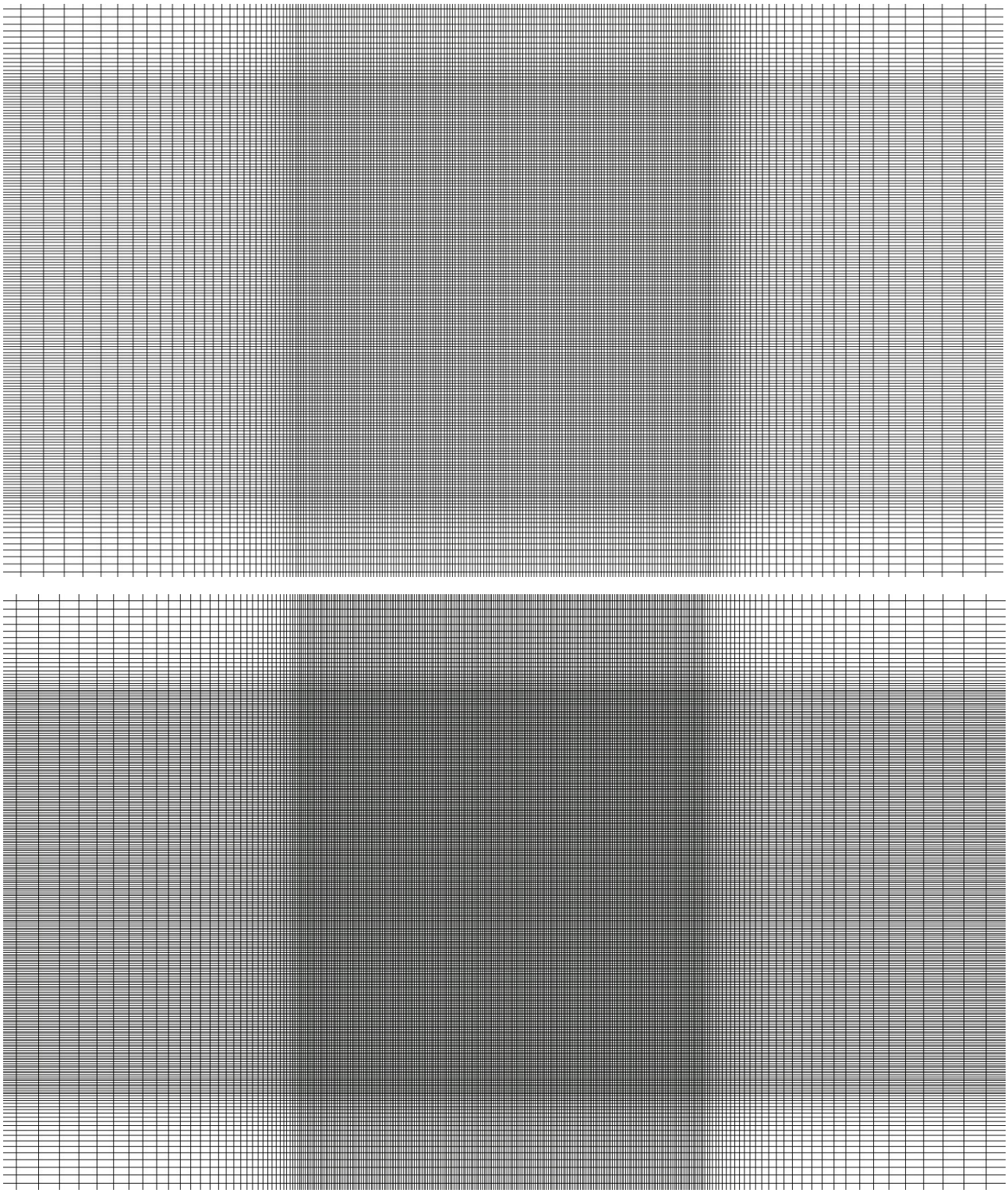

Figure A01. Three meshes that have been utilized in the simulations from the top view

Table TA01. Details of the applied meshes

Parameter	**Mesh 1**	**Mesh 2**	**Mesh 3**
Mesh size	$0.166667\ mm$	$0.083333\ mm$	$0.055556\ mm$
Maximum aspect ratio	40.0695 Cells with maximum aspe[2]	28.0307[2]	28.7873[2]
Mean volume cell	$1.717776{\cdot}10^{-11}\ m^3$	$1.717163{\cdot}10^{-11}\ m^3$	$1.717050{\cdot}10^{-11}\ m^3$

[2] Cells with maximum aspect ratio are located in the bottom glass (1) or in the NOA-61 zone (3)

Orthogonal quality	1.0	1.0	1.0
Number of cells	1314332	3875328	7867008

Table TA02. Richardson- and Roache-extrapolated parameters after 30 seconds of irradiation

Extrapolate error		**Mesh 1 – Mesh 2**	**Mesh 2 – Mesh 3**	$t_{s1}\_ t_{s2}$	$t_{s2}\_ t_{s3}$
$\|\epsilon\|$	*max*	0.050368645 %	0.009325662 %	0.088021221 %	0.073893865 %
	mean	0.069894595 %	0.020863796 %	0.017556023 %	0.010783518 %
$f_{h=0}$	*max*	322.43526114 K	322.43161627 K	322.43212863 K	322.43291446 K
	mean	315.49611408 K	315.48450273 K	315.48696179 K	315.48766655 K
$GCI_{(fine)}$	*max*	0.020986936 %	0.009325662 %	0.036675509 %	0.017593777 %
	mean	0.029122748 %	0.020863796 %	0.007315010 %	0.002567504 %
f_{ext}	*max*	322.4303321 K		322.44180391 K	
	mean	315.4821112 K		315.48891530 K	

Since the spatial errors decrease below 1% significantly, the second mesh is consumed to repeat the procedure for three timesteps – $t_{s1} = 1.0$, $t_{s2} = 0.5$ and $t_{s3} = 0.2\ ms$. Likewise, the obtained comparison implies the time errors at the maximum 0.1% level. Under the abovementioned results from the figures and the tables A01 and TA01,TA02, the 0.5-ms-second-mesh case has been declared to be spatial and time independent and is shifted to the experimental confrontations.